Reconfigurable near-IR metasurface based on Ge₂Sb₂Te₅ phase-change material

ALEXEJ V. POGREBNYAKOV,[1] JEREMY A. BOSSARD,[1] JEREMIAH P. TURPIN,[1] J. DAVID MUSGRAVES,[2] HEE JUNG SHIN,[1] CLARA RIVERO-BALEINE,[3] NIKOLAS PODRAZA,[4] KATHLEEN A. RICHARDSON,[2] DOUGLAS H. WERNER,[1,6] AND THERESA S. MAYER[1,5,7]

[1]Department of Electrical Engineering, Penn State University, University Park, PA 16802, USA
[2]Townes Laser Institute, CREOL, University of Central Florida, Orlando, FL 32816, USA
[3]Lockheed Martin Corporation, Orlando, FL 32819, USA
[4]Department of Physics and Astronomy, University of Toledo, Toledo, OH 43606, USA
[5]Virginia Polytechnic Institute and State University, Blacksburg, VA 24060, USA
[6]dhw@psu.edu
[7]tsmayer@exchange.vt.edu

Abstract: A reconfigurable metasurface made of Ge₂Sb₂Te₅ phase-change material was experimentally demonstrated in the 1.55 μm wavelength range. A nanostructured Ge₂Sb₂Te₅ film on fused silica substrate was optimized to switch from highly transmissive (80%) to highly absorptive (76%) modes with a 7:1 contrast ratio in transmission independent of polarization, when thermally transformed from the amorphous to crystalline state. The metasurface was designed using a genetic algorithm optimizer linked with an efficient full-wave electromagnetic solver.

1. Introduction

Initial work on metamaterials focused on the development of structures based on metallic resonators [1] that has resulted in the fabrication of left-handed materials with negative effective permittivity and permeability. By now, the study of metamaterials and their two-dimensional counterparts, known as metasurfaces, has grown to encompass various macroscopic composites of periodic or non-periodic subwavelength structures whose function arises from a combination of the metamaterial structure and constituent materials composition and properties [2–4]. Recently, nanofabrication techniques have enabled the creation of metamaterials operating in the optical (near infrared (IR)) frequency range [5]. Unique properties of the optical metamaterials have been investigated with the aim to create perfect lenses [6,7], flat collimating lenses [8], invisibility cloaks [9,10], near perfect absorbers [11,12], and other devices for light propagation control [5].

Expanding upon the variety of metamaterials with static responses, there is a growing interest in developing reconfigurable metamaterials that would provide an alterable electromagnetic response as a result of changing the properties of a component material (see. *e.g.*, reviews [13,14]). The availability of such reconfigurable metamaterials would greatly enhance the possibility of their employment in practical applications. As an intermediate step on the way from metamaterials with fixed frequency response to fully reconfigurable artificially structured materials, tunable metamaterials have been created with a limited range of the adjustable frequency response. In the mid- or near IR, the frequency response of the metamaterials was controlled using liquid crystals [15–19] or phase change materials (PCM) such as vanadium oxide [20–23] or chalcogenide alloys (*e.g.*, refs [24–30].). Some limitations of these previous designs stem from the choice of the tuning constituents used in fabrication. For instance, liquid crystal devices have relatively slow switching speeds and demonstrate strong anisotropic behavior. VO₂ exhibits a very fast insulator-to-metal phase transition but has a low (68 °C) phase switching temperature. In comparison with other PCMs,

chalcogenide alloys offer a number of benefits. Many chalcogenide alloys can undergo thermally, electrically, or optically controlled reversible phase transitions between amorphous and crystalline states with an associated large change in the optical and electrical characteristics. Chalcogenide alloys also offer advantages for fabrication due to their thermal and environmental stability, a broad operating temperature range, and the adjustability of their properties and operational wavelengths through composition modification, as dictated by a specific application [31–33].

A distinctive feature shared by most of the previously engineered tunable structures utilizing PCMs based on chalcogenide alloys, is that their tuning components (continuous layers of PCM) were hybridized with the metamaterials, *i.e.*, they only changed the resonance conditions of the framework metamaterials (*e.g.*, refs [24–28].). Here, we adopt another approach to making a reconfigurable photonic metasurface, in which the resonating medium is the nanostructured $Ge_2Sb_2Te_5$ (GST) chalcogenide alloy layer *itself* and another medium is not required to change the resonance. A similar approach was utilized in [29] where a one-dimensional metasurface was etched in the GST film. In [30], the simulations of a two-dimensional metasurface based on the GST film were presented. A unique optical response of the structure in the near IR is achieved in the present work [34], which demonstrates two disparate filter functions as a result of changing the structural phase of the chalcogenide film. Employment of the amorphous (dielectric) GST material where displacement currents act similarly to conduction currents in metallic metamaterial structures allows avoidance of losses inherent to metals at optical frequencies [35].

2. $Ge_2Sb_2Te_5$ film deposition and characterization

The reconfigurable near-IR metasurface involves a nanostructured GST PCM film on a double side polished fused silica wafer. The 150-nm-thick GST films were deposited by thermal evaporation of ground pieces of the GST ingot at room temperature at a rate of $0.15 \div 0.25$ nm/s. The GST ingot for the evaporation was fabricated from high purity chemical elements (99.999% each, Alfa Aesar) batched into a fused silica ampoule inside a nitrogen-purged glove box. Prior to sealing, the material components and silica ampoule were kept under high vacuum ($\sim 10^{-4}$ Torr) at 90 °C for 4 hours in order to remove any residual moisture. The sealed ampoule was heated to 950 °C and then kept at that temperature for 15 hours in a rocking furnace to provide homogenization of the melt. The ampoule was quenched in liquid nitrogen that produced a polycrystalline ingot.

The elemental composition of the films determined by energy-dispersive X-ray spectroscopy (EDS) was found to be the same as the composition of the bulk target alloy from which they were prepared. EDS was performed using a Hitachi S-3400-2 Variable Pressure SEM with a liquid nitrogen cooled EDS attachment using an accelerating voltage of 20 kV.

As-deposited GST thin films were amorphous as verified by X-ray diffraction (XRD) and electrical resistance measurements. The XRD patterns of the films were collected in the Bragg-Brentano configuration using a PANalyticalX'Pert Pro Materials Research Diffractometer with Cu-Kα radiation. To induce a phase transformation from amorphous to one of the crystalline states, the films were subjected to a heat treatment using Alwin 21 AG610 Rapid Thermal Annealing (RTA) System in N_2 flow for 10 sec. Figure 1(a) shows the XRD scans for the as-deposited amorphous GST film (lower spectrum) as well as for the films crystallized by RTA at 170 °C (middle spectrum) and at 370 °C (upper spectrum). The curves are shifted along the vertical axis for clarity. The reflections in the middle spectrum correspond to the face-centered cubic (fcc) structure (Fig. 1(b)) [36, 37], whereas the reflections in the upper spectrum match the hexagonal structure of the GST material [38]. Only (00*l*) reflections are present in the spectrum for the film with hexagonal lattice, indicating a preferred (*c*-axis) orientation of the crystalline structure.

The GST thin films in the amorphous and crystalline states were also studied using Raman scattering in a micro-Raman configuration. The studies were performed using a Bruker

Senterra Raman Microscope (100x objective) at the excitation wavelength of 785 nm. The integration time was 90 sec. A high homogeneity of the films across the 3-inch diameter substrates was confirmed by measuring the Raman scattering at different locations on the films. The Raman scattering spectra for the amorphous and crystalline GST films are presented in Fig. 1(c). The main peak positions in the Raman spectra for the amorphous state (125 and 153 cm^{-1}) and fcc crystalline state (109 and 165 cm^{-1}) agree well with the results of *ab initio* molecular dynamic simulations [39]. These peaks are due to vibrations of defective octahedra formed by Te, Sb, and a majority of the Ge atoms. A broadening of the Raman spectrum for the crystalline state compared to the one for the amorphous state is explained [39] by a larger spread in the Ge-Te and Sb-Te bond lengths when the PCM is in the crystalline state because of disorder introduced by about 20% of vacancy sites in the Ge/Sb sub-lattice [40].
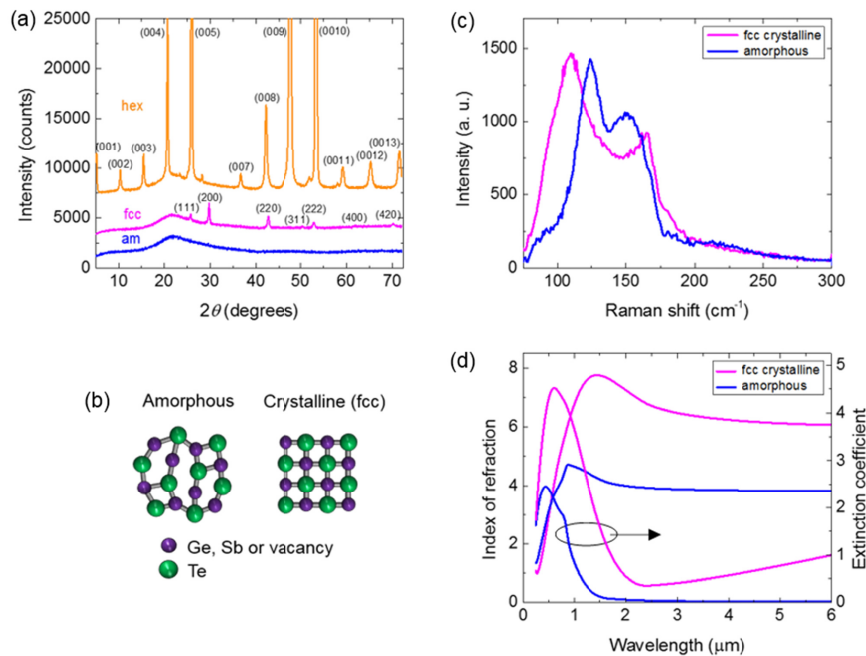

Fig. 1. (a) X-ray diffraction spectra of the 150-nm-thick GST films. Measurement results are shown for samples that are amorphous (lower spectrum), crystallized at 170 °C (middle spectrum) and at 370 °C (upper spectrum). The assigned reflections indicate the formation of the fcc structure (middle curve) and the hexagonal structure (upper curve) in the films. The curves are shifted in the vertical direction for clarity. (b) Schematic representation of the GST film structure transformation from amorphous to fcc crystalline state. (c) Raman scattering spectra for amorphous and crystalline GST films. (d) Measured complex refractive index of amorphous and crystalline (fcc structure) GST films in the near- to mid-infrared range.

To determine the complex index of refraction, N ($N = n + ik$, n – refractive index, k – extinction coefficient), of the GST PCM films, spectroscopic ellipsometry measurements were performed. The ellipsometric spectra were collected at room temperature *ex situ* at four angles of incidence (50°, 60°, 70°, 80°) using variable-angle single rotating compensator Fourier transform infrared [41] and dual rotating-compensator multichannel spectroscopic ellipsometers [42] over spectral ranges from 0.2 to 0.75 eV and 0.75 to 5.15 eV, respectively. All ellipsometric spectra were fit over the 0.2 to 5.15 eV spectral range simultaneously. Spectra in N and microstructural parameters were extracted using a least squares regression analysis and an unweighted error function to fit the experimental ellipsometric spectra based

on an optical model consisting of a semi-infinite fused silica substrate / GST film / surface roughness. The surface roughness was represented by a Bruggeman effective medium approximation of 0.5 void + 0.5 film material fractions. The parameterization of N included combinations of Sellmeier, Lorentz, Tauc-Lorentz, Gaussian, and Drude (for the films in the crystalline state) oscillators. Oscillator parameters as well as thicknesses of the GST film and the surface roughness layer were used as fitting parameters. Figure 1(d) shows the wavelength dependence of n and k for the amorphous and fcc crystalline states of the films that agree well with the GST material parameters reported in Ref [43]. Here, the crystalline phase has higher values of n and k than the amorphous phase, which corresponds to differences in the chemical bonding in the films before and after the phase transition [32,43–45]. It should be noted that some change in the surface roughness (~7 nm increase) of the GST films after the phase transformation from the amorphous to crystalline state was determined using ellipsometry. This increase of the surface roughness is too small to influence the optical properties of the films at the device working wavelength.

3. Metasurface design and fabrication

A large difference in the complex index of refraction for the amorphous and crystalline phases of the GST PCM can be leveraged to create reconfigurable metamaterials or metasurfaces with specific properties that depend on the state of the constituent PCM [46]. The specific goal in the present study was to design a metasurface whose response in the IR (1.55 μm wavelength range) could be reconfigured from high transmission when the PCM is in the amorphous state to high absorption when it is in the fcc crystalline state. To achieve this goal, a robust genetic algorithm (GA) optimizer [47] was employed to create a pixelized pattern in the GST layer deposited on the fused silica substrate. Within the periodic unit cell, the PCM layer was subdivided into an 8 × 8 grid of pixels and represented by 10 unique binary bits using 8-fold symmetry. Enforcing 8-fold symmetry in the design maintains polarization independence and contracts the parameter search space by reducing the number of bits required to encode the unit cell pattern. The encoding for a single triangle in the 8-fold symmetric unit cell shown in Fig. 2(a) is "0011,001,01,1," where "0" represents a "No GST" pixel and "1" represents a "GST" pixel. Furthermore, fabrication constraints that remove isolated pixels and diagonal connections in the geometry were enforced on the unit cell structure. The *Cost* function used in the GA to evaluate the overall performance of the metasurface structure is given by

$$Cost = -dB\{T(Am)\} - dB\{\sqrt{1 - R(Cr) - T(Cr)}\} \tag{1}$$

where the transmittance T and reflectance R for amorphous Am and fcc crystalline Cr phases, respectively, were calculated for the infinite planar array of unit cells by linking the optimizer with an efficient full-wave electromagnetic solver based on the periodic finite element-boundary integral (PFEBI) method [48]. In addition, the *Cost* function was calculated for a range of wavelengths around 1.55μm, recording the best value in the range. The measured n and k values for the amorphous and fcc crystalline phases shown in Fig. 1(d) were used to model the PCM film in the *Cost* evaluation.

The GA evolved the unit cell size, GST layer thickness, and pattern, converging to a structure illustrated in Fig. 2(a,b) as the best candidate design for a reconfigurable transmission/absorption metasurface subject to the fabrication constraints and the *Cost* function defined in (1). The predicted scattering spectra from the metasurface shown in Fig. 2(c,d) reveal a high transmission peak of 82.1% in the amorphous state of the PCM and a high absorption maximum of 82.4% in the fcc crystalline state, indicating that the optimized structure meets the specified reconfigurable metasurface design criteria.

The 4 × 4 mm^2 samples of the GST-based metasurface with the pattern optimized by the GA as shown in Fig. 2(a,b), were fabricated using e-beam lithography and lift-off techniques. The patterns were exposed on a positive electron beam resist (Nippon ZEP 520A) spun onto a

fused silica wafer using a Leica EBPG5-HR E-Beam Writer. The sample fabrication began with calibrating the exposure dose by preparing a series of small area (300 x 300 μm^2) patterns. These dose array patterns were exposed with different doses from 140 to 260 $\mu C/cm^2$ using 10 $\mu C/cm^2$ increments. After resist development, a 150-nm-thick GST film was deposited by thermal evaporation as described above. The lift-off was carried out by dissolving the resist in MicroChem Nano Remover PG. The exposure settings from the dose array pattern that most closely matched the design specifications were used for the fabrication of the full-size samples. Field emission scanning electron microscope (Leo 1530 FESEM) images of small areas of the pattern in the GST film are presented in Fig. 2(e,f).
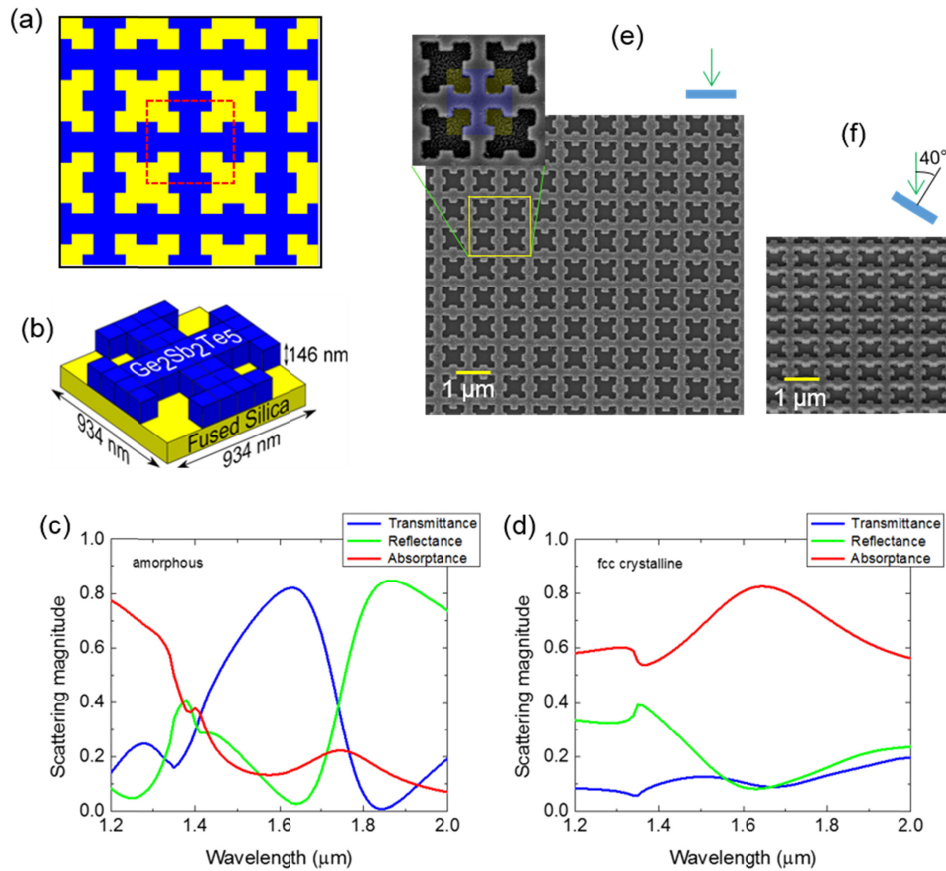

Fig. 2. (a,b) Reconfigurable metasurface pattern designed using the genetic algorithm and PFEBI electromagnetic solver. (c,d) Simulated scattering parameters of the optimized metasurface showing high transmission and high absorption in the 1.55 µm range for the amorphous and fcc-crystalline phases, respectively. (e,f) FESEM images of small areas of the fabricated metasurface sample.

4. Results and discussion

The reflectance and transmittance of the 4 × 4 mm^2 reconfigurable metasurface prototypes were measured at normal incidence using a Bruker IFS 66/S Fourier-Transform Infrared Spectrometer at normal incidence with unpolarized light before and after the patterned GST films were transformed from amorphous to fcc crystalline states. The spectrometer was equipped with a liquid nitrogen cooled mercury-cadmium-telluride detector. To measure the reflectance at near-normal incidence (< 1° off normal), a custom setup composed of mirrors

and a beam splitter was used. The absolute reflectance data were obtained by referencing the sample reflectance to that of an Au mirror. For verification, the absolute reflectance measurements of the reconfigurable metasurface prototype were also carried out on a Perkin-Elmer Lambda 950 UV-Vis-NIR Spectrophotometer using a Universal Reflection Accessory (URA). In order to measure the optical properties of the small-size dose array patterns, a Hyperion 3000 FT-IR microscope was used.

The measured spectra are shown in Fig. 3(a-c). These data demonstrate that at the wavelength where the transmittance undergoes a dramatic change, when the PCM is transformed from an amorphous to a crystalline state, there is only a minor change in the reflectance. Therefore, the fabricated reconfigurable metasurface switches from a highly transmissive to a highly absorbing condition in the targeted 1.55 μm wavelength range. The metasurface prototype demonstrates a peak absorptance of 75.8% when the GST layer is in the crystalline state and a transmittance modulation from 80.1% to 10.7% corresponds to a contrast ratio of 7.5:1. We note that the absence of a continuous metal layer integrated with the metasurface structure makes it considerably more transmissive at resonance when the GST layer is in the amorphous state compared to tunable structures studied in other works where such a layer was a necessary component (e.g. Au in [24,25,28]). We note also that applying antireflection coatings will further improve the structure transmittance. A comparison of the measurement and simulation results shows a good overall agreement in the data. For the same unit cell design, a fine adjustment of the wavelength position of the spectral features is possible by changing the e-beam lithography exposure parameters and/or pattern pixel size which result in an alteration of the pattern sizes and corresponding shift in the spectral position of the transmission and reflection maxima as shown in Fig. 4.
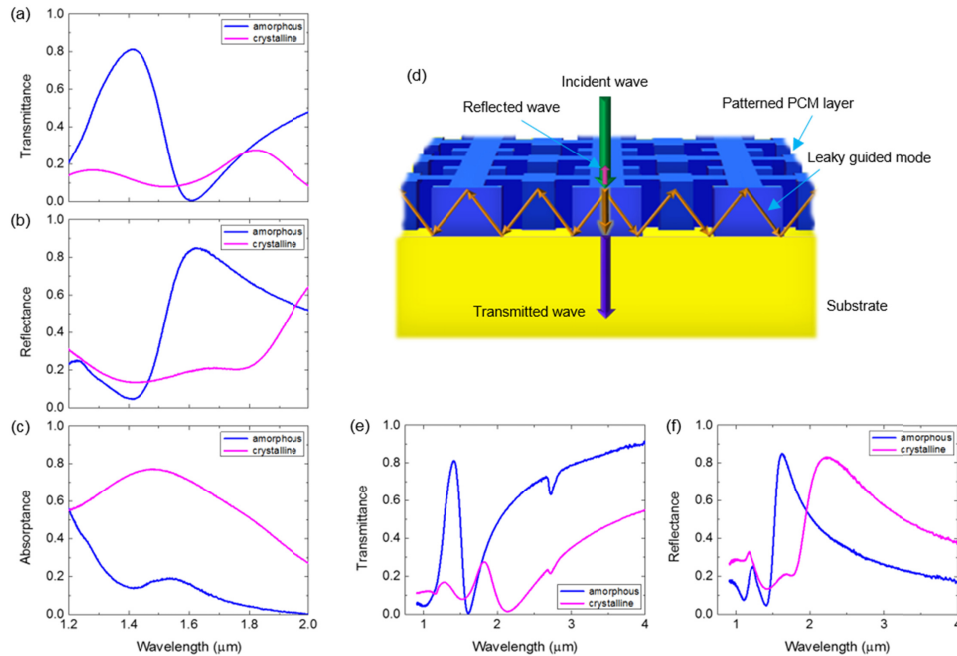

Fig. 3. (a-c) Experimental transmittance, reflectance, and calculated absorptance spectra for the metasurface with GST PCM layer in amorphous and crystalline states. (d) Illustration (using ray tracing) of physical mechanisms leading to the resonant transmission and reflection in the developed metasurface. The leakage of the guided mode is not shown. (e-f) Experimental transmittance and reflectance shown in the broader wavelength range to demonstrate the red-shift of the resonance peaks.

The resonant increase of transmission in the structure (Fig. 3(a)) when the GST material is in the amorphous state is determined by a leaky guided mode resonance induced by the periodic pattern of air voids within the GST PCM layer [49,50]. The average dielectric constant of the patterned PCM layer is higher than those of the cover (air) and the substrate, therefore the patterned layer acts simultaneously as a diffraction grating and a waveguide. Inside the patterned GST layer, the first diffracted orders (± 1) excite guided modes when proper phase matching conditions [51] are met (Fig. 3(d)). The grating formed by patterning the GST layer makes the guided modes leaky which brings about a radiation from the PCM layer extending into the air and substrate [52]. As a result of the interaction between the incident wave, waveguide modes, and radiation fields, as well as the wavelength-dependent probability of the guided mode excitation, the structure provides a resonant response. The structure period, L, satisfies the conditions: $\lambda_R/n_{avg} < L < \lambda_R/n_s$, λ_R/n_c, where λ_R is the resonance wavelength, n_{avg} is the average index of the patterned GST layer, and n_s and n_c are refractive indices of the substrate and cover (air). Thus, the patterned GST layer is a high spatial frequency grating and there are no diffraction orders (except for the zeroth order) in the transmitted light which improves the filter efficiency. The two-dimensionality of the pattern with 90° rotational symmetry makes the response polarization-independent.
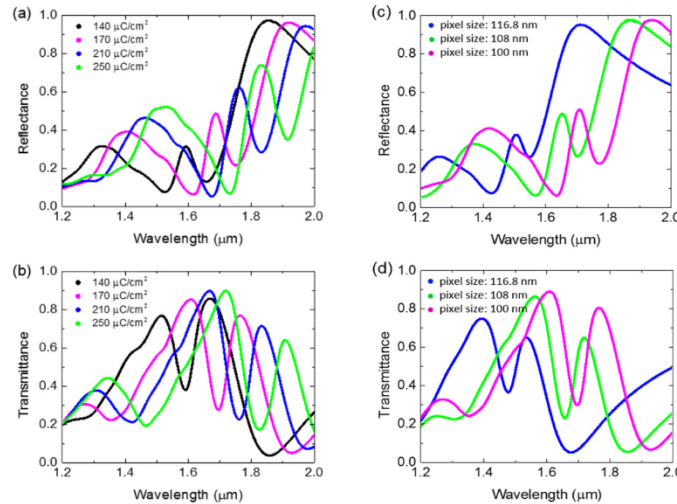

Fig. 4. Reflectance and transmittance spectra of the 300 × 300 μm^2 metasurface patterns formed in the amorphous $Ge_2Sb_2Te_5$ films using: (a), (b) different e-beam exposure doses (the same structure period) and (c), (d) different pixel sizes (variable structure period) as indicated in the insets. The spectra were taken at 20° incidence using the FT-IR microscope.

As noted above, the metasurface pattern design was optimized in such a way that the reflectance is low in both amorphous and crystalline states. This is achieved by shifting the reflection peak to the longer wavelengths upon transforming the patterned GST layer to the crystalline state (see Fig. 3(e,f) where the transmittance and reflectance spectra are shown in a broader wavelength interval compared to Fig. 3(a-c)). The transmission peak also becomes red-shifted and decreases due to higher absorption in the crystalline GST material. In the fcc crystalline phase the GST is conducting – a resistivity $\rho = 2.4$ mΩ-cm was found using the Drude term in the dielectric function determined by ellipsometry. The red-shift of the transmittance and reflectance maxima represents approximately a 1.3 times increase in the vacuum wavelength. This increase is associated with the change in the guided mode wavelength that was brought about by the increase in the refractive index induced by the phase transformation from amorphous to crystalline states. However, the change in the refractive index alone (~1.85 times) would produce a still higher red-shift. It is moderated by

a decrease (~1.5 times) of the GST film thickness when its phase is transformed from amorphous to crystalline.

As a comparison, an optimization of the unpatterned GST layer was carried out to obtain high transmission in its amorphous state and high absorption in the fcc crystalline state. The simulated transmittance, reflectance, and absorptance spectra for an optimized homogeneous 200-nm-thick GST layer in the amorphous and fcc crystalline states are shown in Fig. 5. One can see from Fig. 5(b,c) that the unpatterned 200-nm-thick GST layer provides a transmittance of 77.3% and an absorptance of about 39.5% in the amorphous and fcc crystalline states, respectively, at a wavelength of 1.65 μm. At the optimum wavelength of 1.65μm, the scattering from the homogeneous GST layer was simulated for layer thicknesses ranging from 100 nm to 300 nm as shown in Fig. 5(d,e). The strong transmission peak corresponds to a Fabry-Perot resonance at the 200 GST layer thickness. While the Fabry-Perot etalon conditions provide a transmission comparable to the optimized GST metasurface in the amorphous state, the homogeneous slab in the crystalline state is unable to produce the high absorption of the optimized GST metasurface. Furthermore, the reflectance is high (56.3%) in the crystalline state.
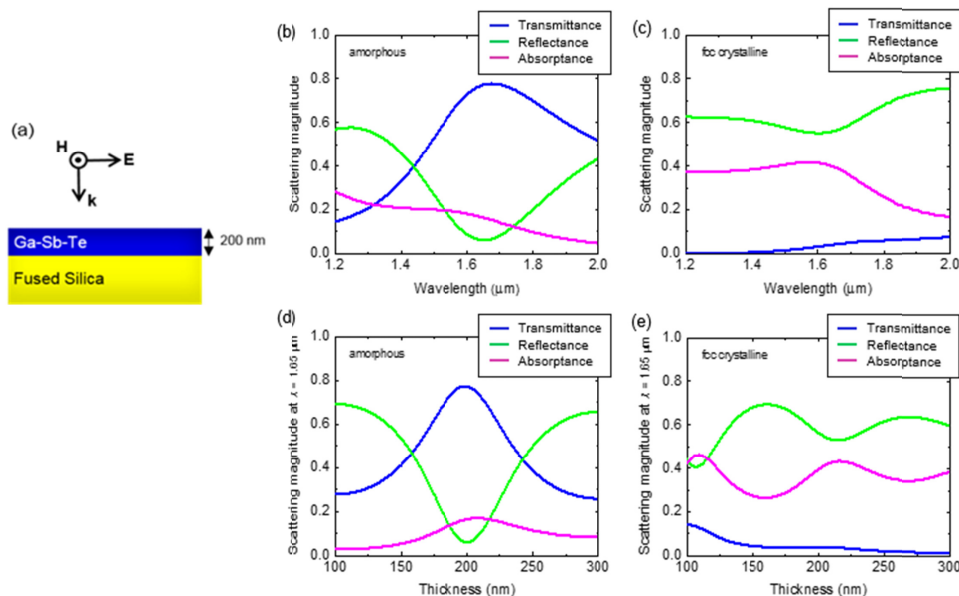

Fig. 5. (a) Homogeneous layer of $Ge_2Sb_2Te_5$ on fused silica substrate optimized to reconfigure from high transmission to high absorption in the amorphous and crystalline states, respectively. (b) Simulated reflectance, transmittance, and absorptance magnitudes for the optimized 200-nm-thick PCM layer in the amorphous and (c) fcc crystalline states. (d) Simulated scattering magnitudes at 1.65 μm wavelength for PCM layer thicknesses ranging from 100 nm to 300 nm in the amorphous and (e) fcc crystalline states.

To illustrate the phenomenon of enhanced resonant transmission and absorption in the developed structure when the patterned GST layer is in its amorphous and crystalline states, respectively, simulations of the electric and magnetic field distributions were carried out. Figure 6 shows the corresponding field distributions obtained from the full-wave model of the metasurface under illumination with normally incident light for the amorphous and fcc crystalline states of GST. The field distributions are shown at the wavelength of 1.7 μm where field enhancement occurs in the amorphous state and at two surrounding wavelengths of 1.4 μm and 1.85 μm, where the field intensities have dropped off significantly (see field magnitude color scale). These field distributions illustrate once again the resonant behavior of

the structure when the PCM is in the amorphous (dielectric) state. The distribution of electric and magnetic field maxima is commensurate with the period of the structure. At $\lambda = 1.7$ μm, the electric field maxima are at the ridges of the holes and the electric field penetrates through the holes (see electric field distributions in Fig. 6, panel c, and in the vertical slice under panel c) providing an increase in the transmission. At higher wavelengths (~1.85 μm) where transmission is low, the reflection from the structure is at a maximum (see Fig. 2(c)). Here, the absorption is relatively small (less than 20%) in the wavelength range of $1.4 - 2$ μm. In the crystalline state of the PCM, an increased intrinsic loss has the effect of reducing the field intensities in the structure as shown for all three wavelengths in Fig. 6(b,d,f), thereby damping the resonant transmission at the corresponding wavelengths. As a result, the absorption increases throughout the band as shown in Fig. 2(d). Thus, the simulations of the electric and magnetic field distributions using a full-wave electromagnetic computational model also attest that the structure provides switching from high transmission to high absorption upon inducing the amorphous to crystalline phase transition in the patterned GST layer.

5. Conclusion

We have presented the design and experimental realization of a reconfigurable metasurface based on a nanostructured $Ge_2Sb_2Te_5$ PCM that changes its response from being highly transmissive to highly absorptive in the near-IR (1.55 µm) wavelength range independent of polarization. Fabrication of the novel design generated using a GA in which the patterned GST layer itself acts as a metasurface demonstrates a considerable improvement in the transmission (80%) of the structure with the GST layer in the amorphous state as compared to previous works. After thermal switching of the nanostructured GST layer to the crystalline state, a high absorption (76%) is attained. A 7.5:1 contrast ratio in transmittance and a 5.4:1 contrast ratio in absorptance were observed while maintaining a low reflectance (5.7% and 13.5% in the amorphous and crystalline states, respectively). This reconfigurable metasurface demonstration using the nanostructured GST film shows great promise as a platform for developing other reconfigurable metasurface devices, as the metasurface response for each PCM state can be tailored by GA optimization according to the application requirements.
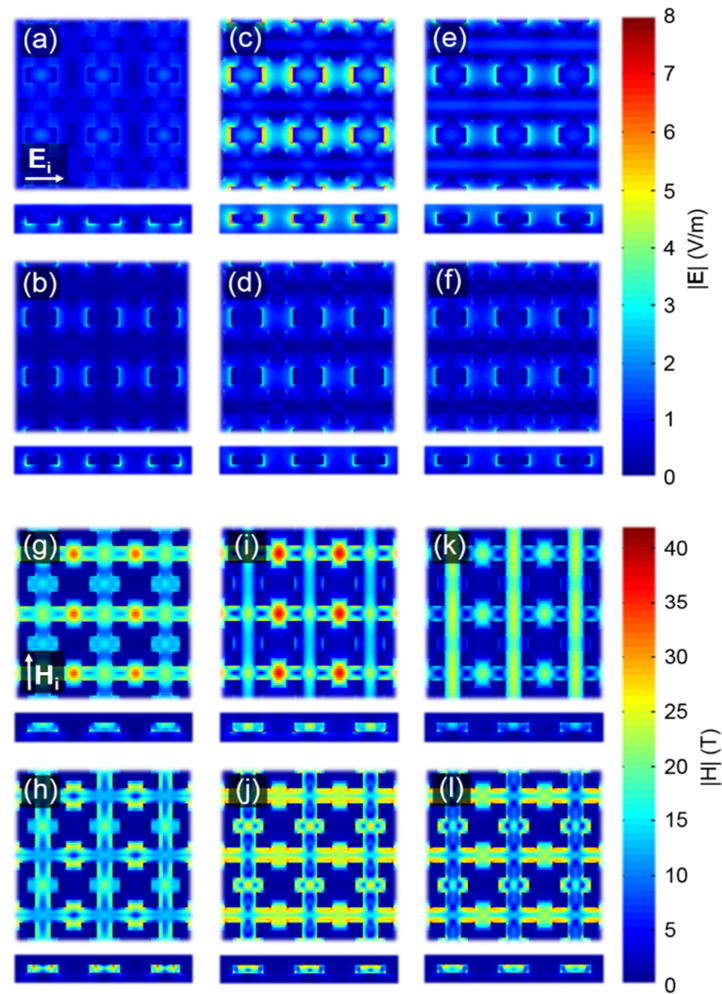
Fig. 6. Simulated electric (a-f) and magnetic (g-l) field magnitudes at three wavelengths for amorphous and fcc-crystalline states of the patterned GST PCM layer of the metasurface. For each panel a horizontal slice through the center of the PCM layer as well as a vertical slice through the edge of the unit cell are shown for a 3 × 3 array of cells. The incident electric and magnetic fields are polarized in the PCM layer plane. λ = 1.4 μm: (a, g) amorphous phase and (b, h) crystalline phase; λ = 1.7 μm: (c, i) amorphous phase and (d, j) crystalline phase; λ = 1.85 μm: (e, k) amorphous phase and (f, l) crystalline phase. Color indicates relative electric and magnetic field magnitudes.

Funding

Acknowledgment

References and links

1. D. R. Smith, W. J. Padilla, D. C. Vier, S. C. Nemat-Nasser, and S. Schultz, "Composite medium with simultaneously negative permeability and permittivity," Phys. Rev. Lett. **84**(18), 4184–4187 (2000).

2. T. J. Cui, R. Liu, and D. R. Smith, "Introduction to Metamaterials," in *Metamaterials*, T. J. Cui, R. Liu, and D. R. Smith, eds. (Springer, 2010).
3. *Theory and Phenomena of Metamaterials*, F. Capolino, ed. (CRC Press, 2009).
4. H.-H. Hsiao, C. H. Chu, and D. P. Tsai, "Fundamentals and applications of metasurfaces," Small Methods **1**(4), 1600064 (2017).
5. A. M. Urbas, J. Jacob, L. D. Negro, N. Engheta, A. D. Boardman, P. Egan, A. B. Khanikaev, V. Menon, M. Ferrera, N. Kinsey, C. DeVault, J. Kim, V. Shalaev, A. Boltasseva, J. Valentine, C. Pfeiffer, A. Grbic, E. Narimanov, L. Zhu, S. Fan, A. Alù, E. Poutrina, N. M. Litchinitser, M. A. Noginov, K. F. MacDonald, E. Plum, X. Liu, P. F. Nealey, C. R. Kagan, C. B. Murray, D. A. Pawlak, I. I. Smolyaninov, V. N. Smolyaninova, and D. Chanda, "Roadmap on optical metamaterials," J. Opt. **18**(9), 093005 (2016).
6. J. B. Pendry, "Negative refraction makes a perfect lens," Phys. Rev. Lett. **85**(18), 3966–3969 (2000).
7. X. Zhang and Z. Liu, "Superlenses to overcome the diffraction limit," Nat. Mater. **7**(6), 435–441 (2008).
8. D.-H. Kwon and D. H. Werner, "Transformation optical designs for wave collimators, flat lenses and right-angle bends," New J. Phys. **10**(11), 115023 (2008).
9. J. B. Pendry, D. Schurig, and D. R. Smith, "Controlling electromagnetic fields," Science **312**(5781), 1780–1782 (2006).
10. J. Valentine, J. Li, T. Zentgraf, G. Bartal, and X. Zhang, "An optical cloak made of dielectrics," Nat. Mater. **8**(7), 568–571 (2009).
11. Z. H. Jiang, S. Yun, F. Toor, D. H. Werner, and T. S. Mayer, "Conformal dual-band near-perfectly absorbing mid-infrared metamaterial coating," ACS Nano **5**(6), 4641–4647 (2011).
12. N. I. Landy, S. Sajuyigbe, J. J. Mock, D. R. Smith, and W. J. Padilla, "Perfect metamaterial absorber," Phys. Rev. Lett. **100**(20), 207402 (2008).
13. G. Oliveri, D. H. Werner, and A. Massa, "Reconfigurable electromagnetics through metamaterials - A review," Proc. IEEE **103**(7), 1034–1056 (2015).
14. S. V. Makarov, A. S. Zalogina, M. Tajik, D. A. Zuev, M. V. Rybin, A. A. Kuchmizhak, S. Joudkazis, and Y. Kivshar, "Light-induced tuning and reconfiguration of nanophotonic structures," Laser Photonics Rev. **11**(5), 1700108 (2017).
15. X. Wang, D.-H. Kwon, D. H. Werner, I. C. Khoo, A. V. Kildishev, and V. M. Shalaev, "Tunable optical negative-index metamaterials employing anisotropic liquid crystals," Appl. Phys. Lett. **91**(14), 143122 (2007).
16. D. H. Werner, D.-H. Kwon, I. C. Khoo, A. V. Kildishev, and V. M. Shalaev, "Liquid crystal clad near-infrared metamaterials with tunable negative-zero-positive refractive indices," Opt. Express **15**(6), 3342–3347 (2007).
17. J. A. Bossard, X. Liang, L. Li, S. Yun, D. H. Werner, B. Weiner, T. S. Mayer, P. L. Cristman, A. Diaz, and I. C. Khoo, "Tunable frequency selective surfaces and negative-zero-positive index metamaterials based on liquid crystals," IEEE Trans. Antenn. Propag. **56**(5), 1308–1320 (2008).
18. D.-H. Kwon, X. Wang, Z. Bayraktar, B. Weiner, and D. H. Werner, "Near-infrared metamaterial films with reconfigurable transmissive/reflective properties," Opt. Lett. **33**(6), 545–547 (2008).
19. W. De Cort, J. Beeckman, R. James, F. A. Fernández, R. Baets, and K. Neyts, "Tuning of silicon-on-insulator ring resonators with liquid crystal cladding using the longitudinal field component," Opt. Lett. **34**(13), 2054–2056 (2009).
20. T. Driscoll, S. Palit, M. M. Qazilbash, M. Brehm, F. Keilmann, B.-G. Chae, S.-J. Yun, H.-T. Kim, S. Y. Cho, N. M. Jokerst, D. R. Smith, and D. N. Basov, "Dynamic tuning of an infrared hybrid-metamaterial resonance using vanadium dioxide," Appl. Phys. Lett. **93**(2), 024101 (2008).
21. M. J. Dicken, K. Aydin, I. M. Pryce, L. A. Sweatlock, E. M. Boyd, S. Walavalkar, J. Ma, and H. A. Atwater, "Frequency tunable near-infrared metamaterials based on VO_2 phase transition," Opt. Express **17**(20), 18330–18339 (2009).
22. J. Rensberg, S. Zhang, Y. Zhou, A. S. McLeod, C. Schwarz, M. Goldflam, M. Liu, J. Kerbusch, R. Nawrodt, S. Ramanathan, D. N. Basov, F. Capasso, C. Ronning, and M. A. Kats, "Active optical metasurfaces based on defect-engineered phase-transition materials," Nano Lett. **16**(2), 1050–1055 (2016).
23. Z. Zhu, P. G. Evans, R. F. Haglund, Jr., and J. G. Valentine, "Dynamically reconfigurable metadevice employing nanostructured phase-change materials," Nano Lett. **17**(8), 4881–4885 (2017).
24. Z. L. Sámson, K. F. MacDonald, F. De Angelis, B. Gholipour, K. Knight, C. C. Huang, E. Di Fabrizio, D. W. Hewak, and N. I. Zheludev, "Metamaterial electro-optic switch of nanoscale thickness," Appl. Phys. Lett. **96**(14), 143105 (2010).
25. B. Gholipour, J. Zhang, K. F. MacDonald, D. W. Hewak, and N. I. Zheludev, "An all-optical, non-volatile, bidirectional, phase-change meta-switch," Adv. Mater. **25**(22), 3050–3054 (2013).
26. T. Cao, L. Zhang, R. E. Simpson, and M. J. Cryan, "Mid-infrared tunable polarization-independent perfect absorber using a phase-change metamaterial," J. Opt. Soc. Am. B **30**(6), 1580–1585 (2013).
27. T. Cao, C. Wei, R. E. Simpson, L. Zhang, and M. J. Cryan, "Fast tuning of double Fano resonance using a phase-change metamaterial under low power intensity," Sci. Rep. **4**(3), 4463 (2014).
28. N. Raeis-Hosseini and J. Rho, "Metasurfaces based on phase-change material as a reconfigurable platform for multifunctional devices," Materials (Basel) **10**(9), 1046 (2017).
29. A. Karvounis, B. Gholipour, K. F. MacDonald, and N. I. Zheludev, "All-dielectric phase-change reconfigurable metasurface," Appl. Phys. Lett. **109**(5), 051103 (2016).

30. C. H. Chu, M. L. Tseng, J. Chen, P. C. Wu, Y.-H. Chen, H.-C. Wang, T.-Y. Chen, W. T. Hsieh, H. J. Wu, G. Sun, and D. P. Tsai, "Active dielectric metasurface based on phase-change medium," Laser Photonics Rev. **10**(11), 1600106 (2016).

31. B. J. Eggleton, B. Luther-Davies, and K. Richardson, "Chalcogenide photonics," Nat. Photonics **5**(3), 141–148 (2011).

32. M. Wuttig and N. Yamada, "Phase-change materials for rewriteable data storage," Nat. Mater. **6**(11), 824–832 (2007).

33. M. Kaes and M. Salinga, "Impact of defect occupation on conduction in amorphous $Ge_2Sb_2Te_5$," Sci. Rep. **6**(8), 31699 (2016).

34. The work described in the present paper was carried out in 2011.

35. J. E. Raynolds, B. A. Munk, J. B. Pryor, and R. J. Marhefka, "Ohmic loss in frequency-selective surfaces," J. Appl. Phys. **93**(9), 5346–5358 (2003).

36. N. Yamada, E. Ohno, K. Nishiuchi, N. Akahira, and M. Takao, "Rapid-phase transitions of $GeTe$-Sb_2Te_3 pseudobinary amorphous thin films for an optical disk memory," J. Appl. Phys. **69**(5), 2849–2856 (1991).

37. I. Friedrich, V. Weidenhof, W. Njoroge, P. Franz, and M. Wuttig, "Structural transformations of $Ge_2Sb_2Te_5$ films studied by electrical resistance measurements," J. Appl. Phys. **87**(9), 4130–4134 (2000).

38. N. Yamada, E. Ohno, N. Akahira, K. Nishiuchi, K. Nagata, and M. Takao, "High speed overwritable phase change optical disk material," Jpn. J. Appl. Phys. **26**(S26–4), 61–66 (1987).

39. G. C. Sosso, S. C. Caravati, R. Mazzarello, and M. Bernasconi, "Raman spectra of cubic and amorphous $Ge_2Sb_2Te_5$ from first principle," Phys. Rev. B **83**(13), 134201 (2011).

40. A. V. Kolobov, P. Fons, A. I. Frenkel, A. L. Ankudinov, J. Tominaga, and T. Uruga, "Understanding the phase-change mechanism of rewritable optical media," Nat. Mater. **3**(10), 703–708 (2004).

41. B. Johns, J. A. Woollam, C. M. Herzinger, J. Hilfiker, R. Synowicki, and C. L. Bungay, "Overview of variable angle spectroscopic ellipsometry (VASE), Part II: Advanced applications," Proc. SPIE **CR72**, 29–58 (1999).

42. C. Chen, I. An, G. M. Ferreira, N. J. Podraza, J. A. Zapien, and R. W. Collins, "Multichannel Mueller matrix ellipsometer based on the dual rotating compensator principle," Thin Solid Films **455–456**, 14–23 (2004).

43. K. Shportko, S. Kremers, M. Woda, D. Lencer, J. Robertson, and M. Wuttig, "Resonant bonding in crystalline phase-change materials," Nat. Mater. **7**(8), 653–658 (2008).

44. J. Hegedüs and S. R. Elliott, "Microscopic origin of the fast crystallization ability of Ge-Sb-Te phase-change memory materials," Nat. Mater. **7**(5), 399–405 (2008).

45. W. Wełnic, A. Pamungkas, R. Detemple, C. Steimer, S. Blügel, and M. Wuttig, "Unravelling the interplay of local structure and physical properties in phase-change materials," Nat. Mater. **5**(1), 56–62 (2006).

46. D. H. Werner, T. S. Mayer, C. Rivero-Baleine, N. Podraza, K. Richardson, J. Turpin, A. Pogrebnyakov, J. D. Musgraves, J. A. Bossard, H. J. Shin, R. Muise, S. Rogers, and J. D. Johnson, "Adaptive phase change metamaterials for infrared aperture control," Proc. SPIE **8165**, 1–9 (2011).

47. R. L. Haupt and D. H. Werner, *Genetic Algorithms in Electromagnetics* (Wiley-IEEE, 2007).

48. T. F. Eibert, J. L. Volakis, D. R. Wilton, and D. R. Jackson, "Hybrid FE/BI modeling of 3-D doubly periodic structures utilizing triangular prismatic elements and an MPIE formulation accelerated by the Ewald transformation," IEEE Trans. Antenn. Propag. **47**(5), 843–850 (1999).

49. S. S. Wang and R. Magnusson, "Theory and applications of guided-mode resonance filters," Appl. Opt. **32**(14), 2606–2613 (1993).

50. S. Tibuleac and R. Magnusson, "Reflection and transmission guided-mode resonance filters," J. Opt. Soc. Am. A **14**(7), 1617–1626 (1997).

51. R. Magnusson and S. S. Wang, "New principle for optical filters," Appl. Phys. Lett. **61**(9), 1022–1024 (1992).

52. I. A. Avrutsky, A. S. Svakhin, and V. A. Sychugov, "Interference phenomena in waveguides with two corrugated boundaries," J. Mod. Opt. **36**(10), 1303–1320 (1989).